Arabian Journal of Chemistry (2023) **16**, 104404

King Saud University

Arabian Journal of Chemistry

www.ksu.edu.sa
www.sciencedirect.com

ORIGINAL ARTICLE

Introducing a new pharmaceutical agent: Facile synthesis of $CuFe_{12}O_{19}$@HAp-APTES magnetic nanocomposites and its cytotoxic effect on HEK-293 cell as an efficient in vitro drug delivery system for atenolol

Kobra Naseri [a], **Elahe Khademi** [b], **Sobhan Mortazavi-Derazkola** [a,*]

[a] *Medical Toxicology and Drug Abuse Research Center (MTDRC), Birjand University of Medical Sciences, Birjand, Iran*
[b] *Student Research Committee, Birjand University of Medical Sciences, Birjand, Iran*

Received 16 July 2022; accepted 5 November 2022
Available online 12 November 2022

KEYWORDS

Hydroxyapatite;
Nanocomposites;
MTT;
Atenolol;
Drug delivery

Abstract In this study, novel $CuFe_{12}O_{19}$@hydroxyapatite magnetic nanocomposites ($CuFe_{12}O_{19}$@HAp MNCs) as controlled target drug delivery were synthesized by ultrasound-assisted precipitation method for the first time. Then, the magnetic substrate was functionalized with APTES ($CuFe_{12}O_{19}$@HAp-APTES MNCs) to increase the efficiency of the drug delivery system. The crystallinity, size, morphology, and composition of the products were determined by FESEM, DLS, BET, TEM, XRD, EDS, and VSM. In order to investigate the drug loading ability of prepared nanocomposites, we chose antihypertensive drug (atenolol) as the model drug. After that, the release behavior of magnetic nanocomposites modified atenolol was investigated under stomach (pH value of 1.5–2) and intestine (pH value of 5.8–6.7) conditions. The results revealed that the highest entrapment efficiency was achieved by $CuFe_{12}O_{19}$@HAp-APTES MNCs (63.1%). Furthermore, the controlled-release potential for $CuFe_{12}O_{19}$@HAp-APTES MNCs was the highest compared with the pure $CuFe_{12}O_{19}$@HAp MNCs. Increased efficiency can be due to the binding of the amine group in APTES with the atenolol drug. The cytotoxicity of the ATL-loaded magnetic nanocomposites (ATL-$CuFe_{12}O_{19}$@HAp-APTES MNCs) was investigated on the HEK-293 cell

* Corresponding author.
E-mail addresses: S.mortazavi23@yahoo.com, Sobhan.mortazavi@bums.ac.ir (S. Mortazavi-Derazkola).
Peer review under responsibility of King Saud University.

Production and hosting by Elsevier

https://doi.org/10.1016/j.arabjc.2022.104404

line using MTT assay. Based on the results, we concluded that the synthesized magnetic nanocomposites could be effective vehicles for the sustained delivery of atenolol as an antihypertensive drug.

1. Introduction

In the recent decade, nanomaterials are playing a critical role in scientific research, including environmental (Hışır et al., 2022; Khormali et al., 2021; Shirzadi-Ahodashti et al., 2020), biological (Saejung et al., 2022; Ebrahimzadeh et al., 2021; Hashemi et al., 2022), pharmacy (Khushbu, 2021), and medicine (Mohammadzadeh et al., 2019). In recent years, a lot of research has been done in the field of preparation and identification of nanomaterials and their use in therapeutic applications. One of the most interesting uses of nanoscience in biomedical is the use of nanomaterials as drug delivery systems, that target the drug to an area of interest. Different compounds have been utilized in drug-delivery applications such as SiO_2/ZnO (Zhang et al., 2022), SiO_2/γ-Fe_2O_3 (Wei et al., 2017), PLA/TiO_2 (Salahuddin et al., 2020), Fe_3O_4@APTES/Cs/TG (Shafiee et al., 2019), ZnO/SBA-16 (Fekri et al., 2022). Atenolol as one of the famous drugs can be a good option for combination with nanocarriers.

Atenolol drug (ATL; $C_{14}H_{22}N_2O_3$; Fig. 1) is a p-adrenoceptor antagonist currently applied for the treatment of hypertension, angina, heart failure, and myocardial infarction (Thadikonda et al., 1995; Adhikari et al., 2010). About fifty percent of this drug is absorbed from the gastrointestinal tract (oral dose). Therefore, it is essential to design an appropriate drug delivery system with few side effects (such as atenolol).

In recent years, hexaferrite compounds ($MFe_{12}O_{19}$) have attracted the attention of researchers owing to their unique properties. The hexaferrite are very useful and applied in various fields, including permanent magnets, plastic magnets, catalysts and high-density magnetic recording media (Ansari et al., 2016; Kaur et al., 2022; Khan et al., 2022). The hexaferrite compounds were discovered in the 1950 s (Ansari et al., 2016). However, it is still interesting for researchers to study the properties of these compounds. As mentioned above, the formula of these compounds is $MFe_{12}O_{19}$; M can be a divalent element. Up to now, various nanomaterials of these magnetic compounds have been synthesized such as $PbFe_{12}O_{19}$ (Ansari et al., 2015), $ZnFe_{12}O_{19}$ (Khoobi et al., 2021), $BaFe_{12}O_{19}$ (Thirupathy et al., 2020), and $SrFe_{12}O_{19}$ (Herrault et al., 2021). Therefore, due to the unique properties of these compounds, we decided to introduce a new drug delivery system based on these compounds. Table. 1 presents the magnetic nanocomposites used in drug delivery. Hydroxyapatite compound ($Ca_{10}(PO_4)_6(OH)_2$; HAp) is highly biocompatible, including bio-material that has the same element ratio as natural teeth and bones (Ca:P = 1.67) (Mushtaq et al., 2021). Mechanical, non-inflammatory and bioactive properties are also other characteristics of hydroxyapatite (Abbasi Aval et al., 2016). Thus, because of the close similarity of this compound with the inorganic component of natural bone and pH-sensitive characteristics, the use of this combination in drug delivery systems looks very attractive.

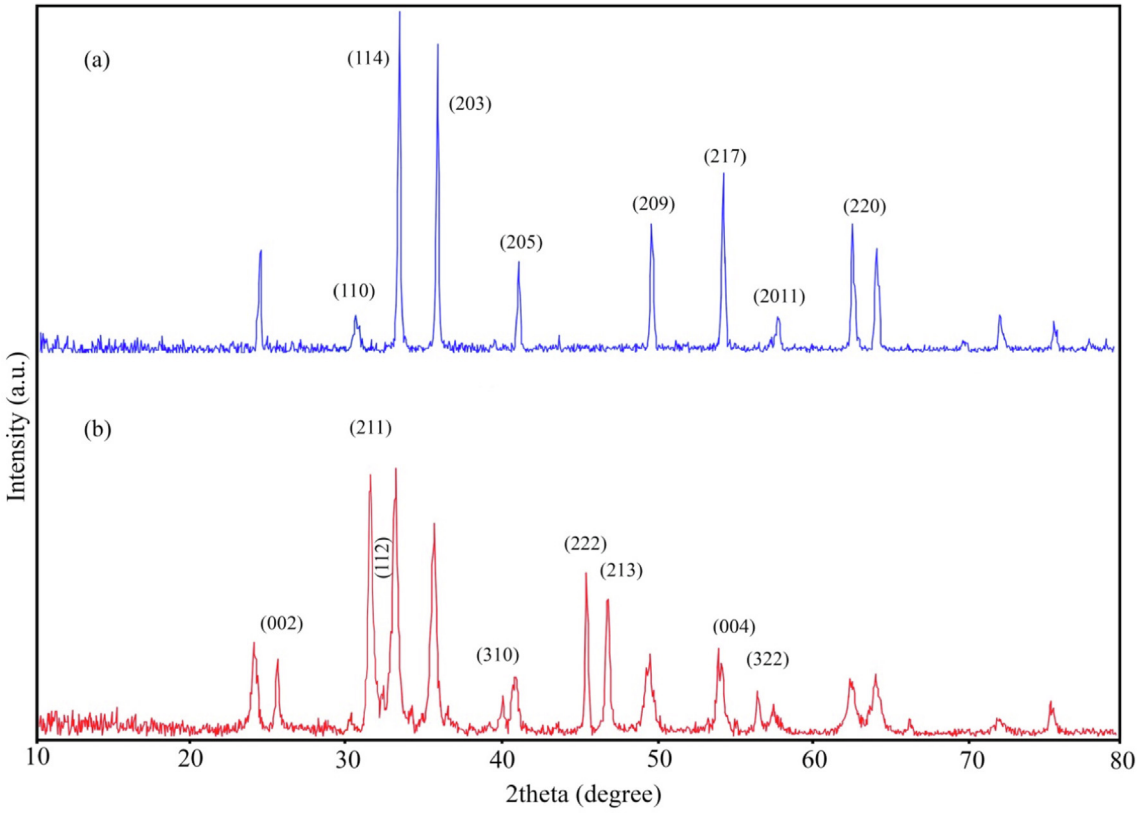

Fig. 1 XRD patterns of (a) $CuFe_{12}O_{19}$ and (b) $CuFe_{12}O_{19}$@HAp MNCs.

Table 1 Magnetic nanomaterials used in drug delivery system.

Sample No	Carrier	Size (nm)	Morphology	Drug	Ref
1	SiO_2@Fe_3O_4	< 100	Spherical	Curcumin	(Asgari et al., 2021)
2	Fe_3O_4@starch-itaconic acid	40	Spherical	Guaifenesin	(Nezami et al., 2020)
3	$CoFe_2O_4$-HAp	85–65	Spherical	Ibuprofen	(Hassanzadeh-Tabrizi et al., 2021)
4	magnetite/silica	21.3–30	Spherical and slightly agglomerate	Doxorubicin	(Taufiq et al., 2020)
5	CMC/PAA/St-Fe_3O_4	25–100	Spherical with core–shell structure	Doxorubicin & 5-fluorouracil	(Mohammadi et al., 2021)
6	$Ce_{4-x}Cs_{2(1+x)}Fe_{5-x}ZnxO_{14+\delta}$	10	Spherical and honeycomb-like	Ciprofloxacin	(Thangaraj et al., 2022)
7	hydroxyapatite-$MgFe_2O_4$	40–100	Spherical and oval	Ibuprofen	(Foroughi et al., 2016)
8	$CoFe_2O_4$	13.2	Spherical	Chlorpheniramine maleate	(Amiri et al., 2017)
9	Fe_3O_4-zeolite	30	Cubic	5-fluorouracil	(Sağir et al., 2016)
10	Fe_3O_4@SiO_2-hydroxyapatite	90–100	Spherical	Sulfasalazine	(Orooji et al., 2020)

In this research, novel $CuFe_{12}O_{19}$@hydroxiapatite nanocomposites were prepared using ultrasound-assisted precipitation method for the first time. Then, the obtained nanocomposites are functionalized with APTES ($CuFe_{12}O_{19}$@HAp-APTES MNCs). The purpose of this research is to investigate the ability of $CuFe_{12}O_{19}$@HAp-APTES MNCs as a novel nanocarrier for atenolol delivery in the stomach and intestine pH (1.5–2 and 5.8–6.7) buffered solutions.

2. Experimental

2.1. Chemical used and characterization

The materials applied in this work include calcium nitrate tetrahydrate ($Ca(NO_3)_2{\cdot}4H_2O$), ammonium hydroxide (NH_4OH), diammonium hydrogen phosphate ($(NH_4)_2HPO_4$), copper (II) nitrate trihydrate $Cu(NO_3)_2{\cdot}3H_2O$; iron (III) nitrate, (3-aminopropyl)triethoxysilane (APTES), methanol, ethanol, and ammonium were purchased from Merck and Sigma-Aldrich Companies and used without any further purification. In reacting materials, all solutions were prepared using distilled water. The concentration of the atenolol loaded into the magnetic nanocomposites was determined using UV–Vis spectrophotometer (BioTek instrument, model Epoch; USA). The XRD was applied to characterize the structure and phase of synthesized products. The crystalline structure of $CuFe_{12}O_{19}$ and $CuFe_{12}O_{19}$@hydroxyapatite with X-ray diffraction were examined by Philips PW 1800 with Cu Kα radiation (2θ = 10°-80°; λ = 1.54 Å). Fourier transform infrared (FTIR) spectroscopic analyses of $CuFe_{12}O_{19}$, $CuFe_{12}O_{19}$@-HAp MNCs, and $CuFe_{12}O_{19}$@HAp-APTES MNCs were performed by PerkinElmer Spectrum TwoTM IR spectrometer; Model L160000U (400–4000 cm^{-1}). Field emission scanning electron microscopy (FE-SEM) and transmission electron microscopy (TEM) images of products were captured using TESCAN BRNO-Mira3 LMU and Zeiss-EM10C-100 KV, respectively.

2.2. Fabrication of $CuFe_{12}O_{19}$ magnetic nanoparticles

Magnetic $CuFe_{12}O_{19}$ nanoparticles were prepared using the previous report with a slight modification (Ansari et al., 2016). Magnetic $CuFe_{12}O_{19}$ nanoparticles were fabrication by reaction between iron nitrate salt and copper nitrate salt in the presence of ammonium hydroxide. For this purpose, 0.5 g of copper nitrate salt was dissolved in distilled water (30 mL). In another container, 3.56 g of iron (III) nitrate was dissolved in 30 mL of distilled water and added to the above solution (the molar ratio of Fe^{3+}:Cu^{2+} was 6: 1). Then, aqueous ammonia hydroxide was added to the above mixture to maintain the pH = 12. After 2 h, the precipitate was collected, washed (three times with distilled water and ethanol), and dried at 70 °C. Finally, the resulting powder was transferred to a furnace and calcined at 900 °C for 2 h.

2.3. Synthesis of $CuFe_{12}O_{19}$@hydroxyapatite nanocomposites ($CuFe_{12}O_{19}$@HAp MNCs)

For the synthesis of hydroxyapatite, diammonium hydrogen phosphate and calcium nitrate salt were taken as precursors of PO_4^{3-} and Ca^{2+} ions, respectively. The $CuFe_{12}O_{19}$@HAp MNCs were synthesized via ultrasound-assisted precipitation route. Initially, 0.3 gr of $CuFe_{12}O_{19}$ was dispersed in 15 mL of ethanol and 15 mL of distilled water under ultrasonic conditions. After that, 0.64 M of calcium nitrate solution and 0.4 M of diammonium hydrogen phosphate solution were prepared in various beakers (the molar ratio of P:Ca was 1:1.6). Next, the mixture solution (phosphate + calcium solutions) was added dropwise to the $CuFe_{12}O_{19}$ solution and adjusted the pH to 12 by adding the ammonium hydroxide (NH_4OH) with intense stirring for 3 h. The final product was washed thoroughly with distilled water and dried overnight at room temperature. $CuFe_{12}O_{19}$@HAp MNCs was obtained by calcining of the precipitate at 500 °C for 2 h.

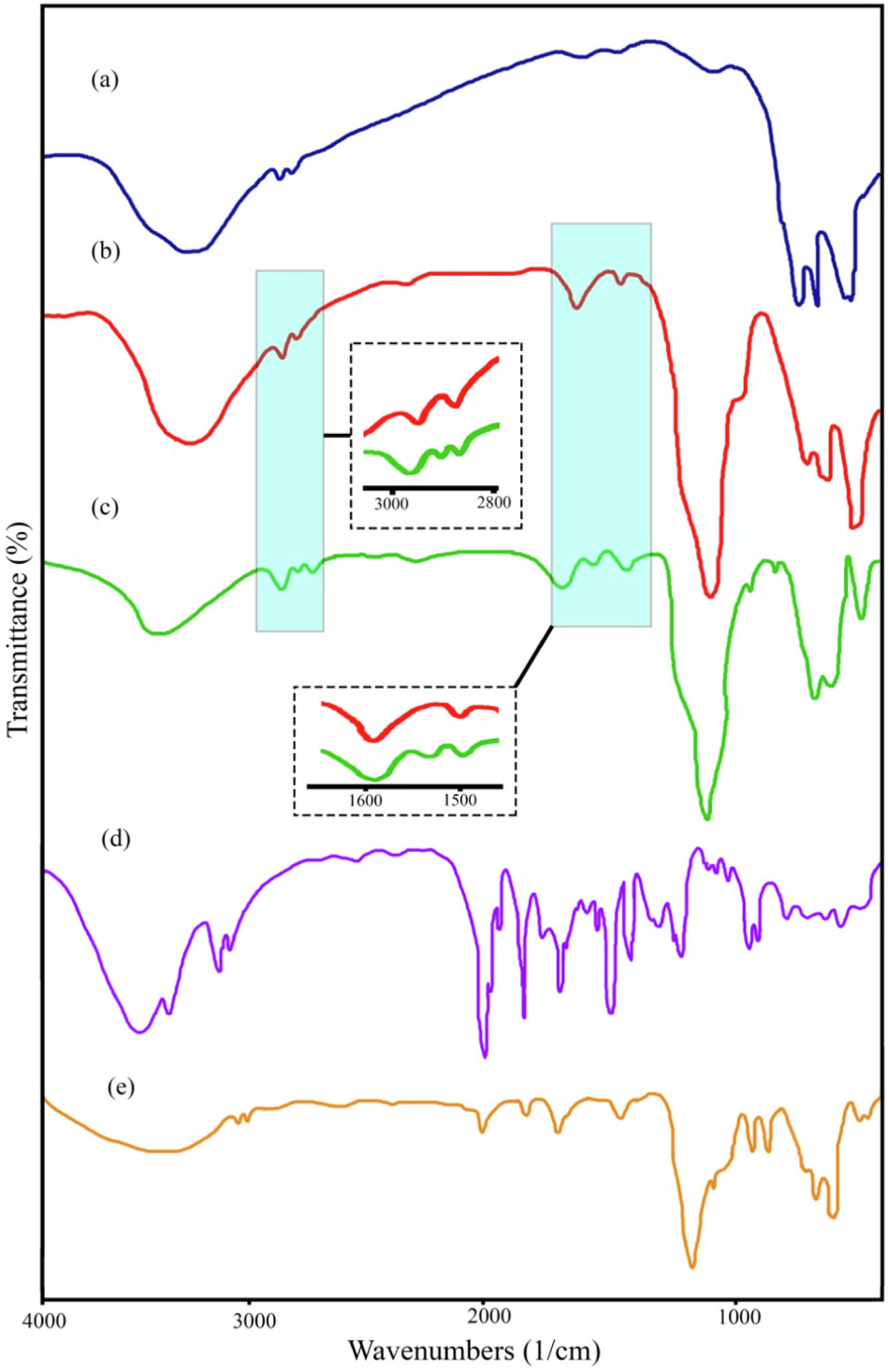

Fig. 2 FT-IR spectra of (a) $CuFe_{12}O_{19}$, (b) $CuFe_{12}O_{19}$@HAp MNCs, (c) $CuFe_{12}O_{19}$@HAp-APTES MNCs, (d) atenolol, and (e) ATL-$CuFe_{12}O_{19}$@HAp-APTES MNCs.

2.4. Modification of magnetic $CuFe_{12}O_{19}$@HAp NCs using APTES ($CuFe_{12}O_{19}$@HAp-APTES MNCs)

The functionalization of $CuFe_{12}O_{19}$@HAp MNCs was carried out based on a previous report with some modifications (Cueto-Díaz et al., 2021). For the functionalization of $CuFe_{12}O_{19}$@HAp MNCs by APTES, 0.5 g of $CuFe_{12}O_{19}$@HAp MNCs was dispersed in 25 mL of toluene by sonicating for 30 min. Next, 1 mL of APTES was added to the solution. The resultant solution was heated at 50 °C and kept under stir-

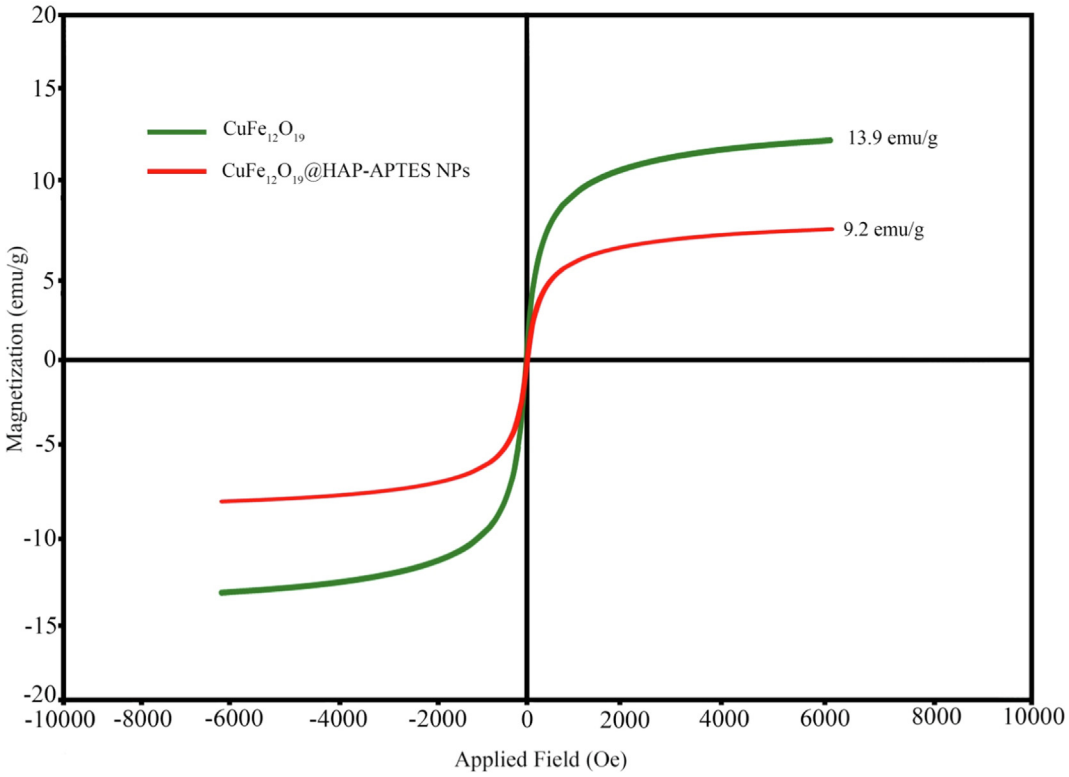

Fig. 3 VSM magnetization curves of $CuFe_{12}O_{19}$, and $CuFe_{12}O_{19}$@HAp MNCs.

ring for 24 h. Finally, APTES functionalized $CuFe_{12}O_{19}$@-HAp MNCs were thoroughly washed and centrifuged three times to remove the excess ions on the surface of product.

2.5. Cytotoxicity of $CuFe_{12}O_{19}$@HAp-APTES MNCs

MTT is a colorimetric assay that determines the viable cells by converting the yellow soluble tetrazolium salt [3-(4,5-dimethyl thiazol-2-yl)-2,5-diphenyltetrazolium bromide] (MTT) to dark insoluble formazan dye. This assay was performed according to the previous instructions (Orooji et al., 2020). Typically, 10^4 HEK-293 cells seeded in a 96-well plate and incubated at 37 °C. Then, 10 µl of the media (RPMI) was removed, and 10 µl of two separate groups ATL-$CuFe_{12}O_{19}$@HAp-APTES MNCs, and free drug at different concentrations (1, 5, 10, 20, 50, and 100 mg/mL) were added to each well. After incubation times at 37 °C for 24 and 48 h at 5 % CO_2 atmosphere, 20 µl of the medium was withdrawn and 20 µl of prepared solution (5 mg of MTT powder in 1 mL of PBS) was added to each well. Untreated cells were chosen as control (blank) group. After 4 h of incubation, medium of each well was removed and 100 µl of dimethyl sulfoxide (DMSO) was added. Absorption was read at 570 nm by ELISA reader.

2.6. Atenolol loading and release

Atenolol as a beta-blocker drug was loaded into the magnetic $CuFe_{12}O_{19}$@HAp MNCs and $CuFe_{12}O_{19}$@HAp-APTES MNCs by immersing (Mortazavi-Derazkola et al., 2016). In the atenolol loading test, some nanocomposites (100 mg) were added to a 5 mL methanolic solution containing methanol and drug (100 mg of drug dissolved in 5 mL of methanol solution) at room temperature under magnetic stirring for 24 h. The atenolol-loaded nanocomposites (ATL-$CuFe_{12}O_{19}$@HAp MNCs and ATL-$CuFe_{12}O_{19}$@HAp-APTES MNCs) were centrifuged at 10000 rpm for 15 min. UV–vis spectroscopy was applied to study the atenolol loading capacity of the prepared nanocomposites at 220 nm. Simulated body fluid (SBF) solution simulated the body-tissue liquid. The ionic composition in the fabricated SBF was as follows: SO_4^{2-}, Mg^{2+}, Cl^-, K^+, Na^+, HCO^{3-}, Ca^+, and HPO_4^{2-} of 0.5, 1.5, 147.8, 5, 142, 4.2, 2.5, and 1 mM, respectively. The in-vitro release of atenolol from ATL-$CuFe_{12}O_{19}$@HAp MNCs and ATL-$CuFe_{12}O_{19}$@HAp-APTES MNCs was investigated at pH = 6.8 (intestinal conditions) and for different time intervals. For this purpose, some magnetic nanocomposites (50 mg) were dispersed into 100 mL of SBF under magnetic stirring. Next, the upper liquid was separated (3 mL) using a pipette and its absorbance intensity was determined at 420 nm. In addition, 3 mL of fresh FBS solution was added.

3. Results and discussion

3.1. Structural analysis

Fig. 1 shows X-ray diffraction analysis (XRD) patterns of as-synthesized ferrites with 1:12 ratios of Cu:Fe ($CuFe_{12}O_{19}$) and $CuFe_{12}O_{19}$@HAp MNCs. Due to the $CuFe_{12}O_{19}$ is one of the newest compounds, the XRD pattern of hexaferrite (Fig. 1a) failed to be identified from among the JCPDS cards. This

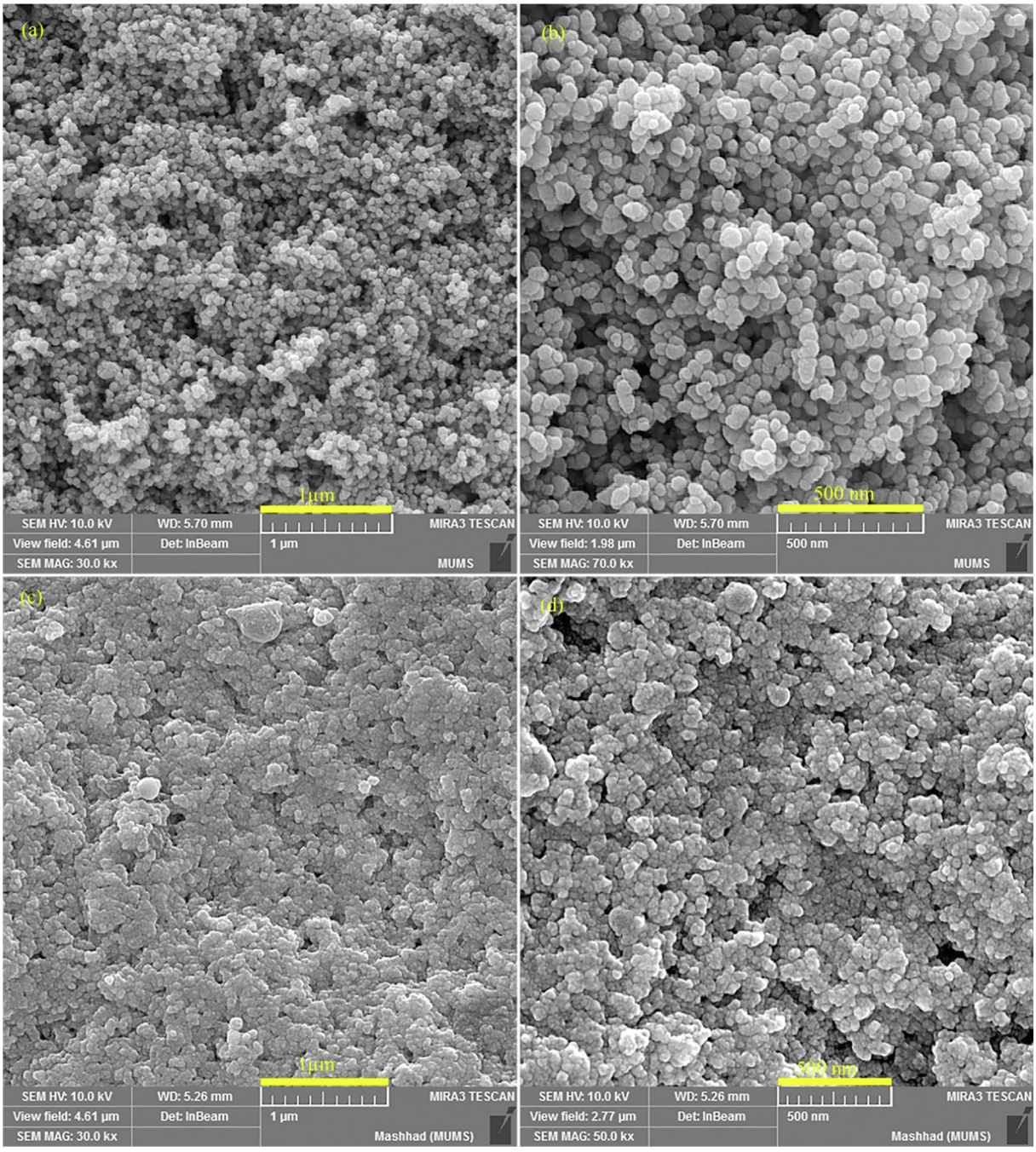

Fig. 4 FESEM images of (a and b) $CuFe_{12}O_{19}$, and (c and d) $CuFe_{12}O_{19}$@HAp MNCs.

result is consistent with previous reports (Mahdiani et al., 2018). The XRD pattern of $CuFe_{12}O_{19}$@HAp MNCs was illustrated in Fig. 1b. In the XRD pattern of $CuFe_{12}O_{19}$@HAp MNCs, the prominent diffraction peaks at 2θ of 25.7°, 31.6°, 39.4°, 46.5°, and 49.8° are related to the (0 0 2), (2 1 1), (3 1 0), (2 2 2) and (2 1 3) crystalline planes of hydroxyapatite, respectively. All diffraction lines are according to what is known as the reference pattern of hydroxyapatite (JCPDS card no. 09–0432) (Saire-Saire et al., 2020; Salimi, 2021). Furthermore, the mean crystallite sizes of 42 nm were calculated about 73 nm using the Scherrer equation (Shirzadi-Ahodashti et al., 2020).

3.2. Fourier-transform infrared spectroscopy (FT-IR)

Fig. 2 shows the FT-IR spectrum of the as-fabricated $CuFe_{12}O_{19}$, $CuFe_{12}O_{19}$@HAp MNCs, $CuFe_{12}O_{19}$@HAp-APTES MNCs, atenolol, and $CuFe_{12}O_{19}$@HAp-APTES-atenolol. The peaks appearing at about 3400 and 1600 cm^{-1} in all spectrums are attributed to the hydroxyl groups (–OH) of water on the surface of products (Shirzadi-Ahodashti et al., 2020; Naghizadeh et al., 2021; Shirzadi-Ahodashti et al., 2021). The absorption bands at 514.7 and 614.3 cm^{-1} were related to Cu–O and Fe-O bonds from the $CuFe_{12}O_{19}$ sample, respectively (Fig. 2a) (Mahdiani et al., 2018). By applying FT-IR, the

purity of the functionalized $CuFe_{12}O_{19}$@HAp MNCs was checked and confirmed. The FT-IR spectrum of $CuFe_{12}O_{19}$@-HAp MNCs is shown in Fig. 2b. The peaks at around 1083.5 and 617.9 cm^{-1} corresponded to the phosphate group and PO_4^{3-}, respectively. The FT-IR spectra showed two weak absorption bands at 1436.2 and 881.6 cm^{-1} related to carbonate and hydrogen phosphate, respectively (Tian et al., 2014; Yang et al., 2010). Fig. 2c shows the weak peaks at about 2918.3 and 1533.2 cm^{-1}, which are related to the C—H stretching of propyl and amine groups, respectively (Orooji et al., 2020). Furthermore, FT-IR sternum of atenolol and $CuFe_{12}$-O_{19}@HAp-APTES-atenolol was showed in Fig. 2d and e. As observed, atenolol drugs were correctly loaded in $CuFe_{12}$-O_{19}@HAp-APTES (see Fig. 3).

3.3. Magnetic measurement

The vibrating sample magnetometer (VSM) analysis was utilized to investigate the magnetic properties of products. The Magnetization property of synthesized magnetic $CuFe_{12}O_{19}$ and $CuFe_{12}O_{19}$@HAp-APTES MNCs was measured at room temperature and revealed in Fig. 2. The saturation magnetization of $CuFe_{12}O_{19}$ and $CuFe_{12}O_{19}$@HAp-APTES MNCs were measured to be 13.9 and 9.2 emu/g, respectively. In 2016, Ansari *et al.*, synthesized $CuFe_{12}O_{19}$ nanostructures. VSM analysis was carried out to check the magnetic performance. The results showed that the synthesized nanostructures had moderate magnetic properties (6 emu/g) (Ansari et al., 2016). As can be seen, the saturation of $CuFe_{12}O_{19}$@HAp-APTES MNCs (13.9 emu/g) was decreased to 9.2 emu/g due to the placement of HAp-APTES on the surface of $CuFe_{12}O_{19}$. Compared to previous results, the synthesized nanoparticles have good magnetic properties. The VSM results showed that the synthesized $CuFe_{12}O_{19}$@HAp-APTES MNCs had promising magnetic properties that could be used as a reusable drug carrier.

3.4. Morphological and elemental analysis

Field-emission scanning electron microscopy (FESEM) and transmission electron microscopy (TEM) analysis were utilized to study the size and morphology of products. The shape and size of the $CuFe_{12}O_{19}$ and $CuFe_{12}O_{19}$@HAp-APTES MNCs were examined by FESEM and TEM, presented in Fig. 4 and Fig. 5, respectively. Based on the FESEM micrographs, the $CuFe_{12}O_{19}$ exhibits a spherical-like and oval-like structure with an average size of 35–50 nm (Fig. 4a and b). The shape and size of the products was confirmed using TEM analysis. As Fig. 5a shows, the morphology of $CuFe_{12}O_{19}$ nanoparticles is spherical, homogenous, and irregular. FESEM observations proved that size and morphology changes occur after deposition of HAp-APTES on the surface of $CuFe_{12}O_{19}$ ($CuFe_{12}$-O_{19}@HAp-APTES MNCs; Fig. 4c and d). The particle size of the product was increased (65–80 nm). Furthermore, when hydroxyapatite was used, the surface morphology changed to a combination of rod and spherical. The rod structure of $CuFe_{12}O_{19}$@HAp-APTES MNCs is due to the hydroxyapatite part of the nanocomposite. Because the product has magnetic properties, TEM observation may induce some aggregation of the magnetic particles (Fig. 5b). Chemical compositions of the products were analyzed using EDS analysis. Elemental analysis of $CuFe_{12}O_{19}$ and $CuFe_{12}O_{19}$@HAp MNCs is shown in Fig. 6. The elemental analysis results of the $CuFe_{12}O_{19}$ showed the presence of copper, iron, and oxygen, confirming the formation of the $CuFe_{12}O_{19}$ (Fig. 6a). The presence of oxygen, copper, iron, calcium, and phosphorus in the $CuFe_{12}O_{19}$@-HAp MNCs spectrum showed that the compound had a high percentage of purity (Fig. 6b).

3.5. DLS and BET analysis

The hydrodynamic diameters and surface charge of the as-prepared products were determined by dynamic light scattering (DLS) and zeta-potential techniques, respectively. The particle size distribution of the $CuFe_{12}O_{19}$ and $CuFe_{12}O_{19}$@HAp-APTES MNCs is presented in Fig. 7a and b. The average diameter of the $CuFe_{12}O_{19}$ and $CuFe_{12}O_{19}$@HAp-APTES MNCs was measured as 30–90 and 60–130 nm. The increase in size confirms the hydroxyapatite deposited on the surface of the $CuFe_{12}O_{19}$ magnetic nanoparticles. Knowing the zeta potential is essential for the characterization of surface properties. Higher zeta potential represents stable dispersion (Darwish et al., 2019). The zeta potential values were −17.6 and −6.1 mV for $CuFe_{12}O_{19}$ and $CuFe_{12}O_{19}$@HAp-APTES

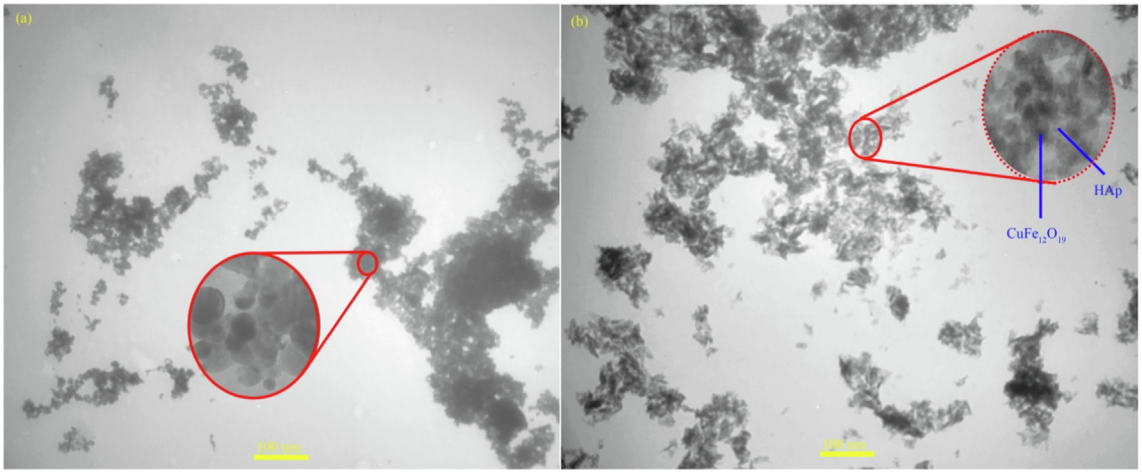

Fig. 5 TEM images of (a) $CuFe_{12}O_{19}$, and (b) $CuFe_{12}O_{19}$@HAp MNCs.

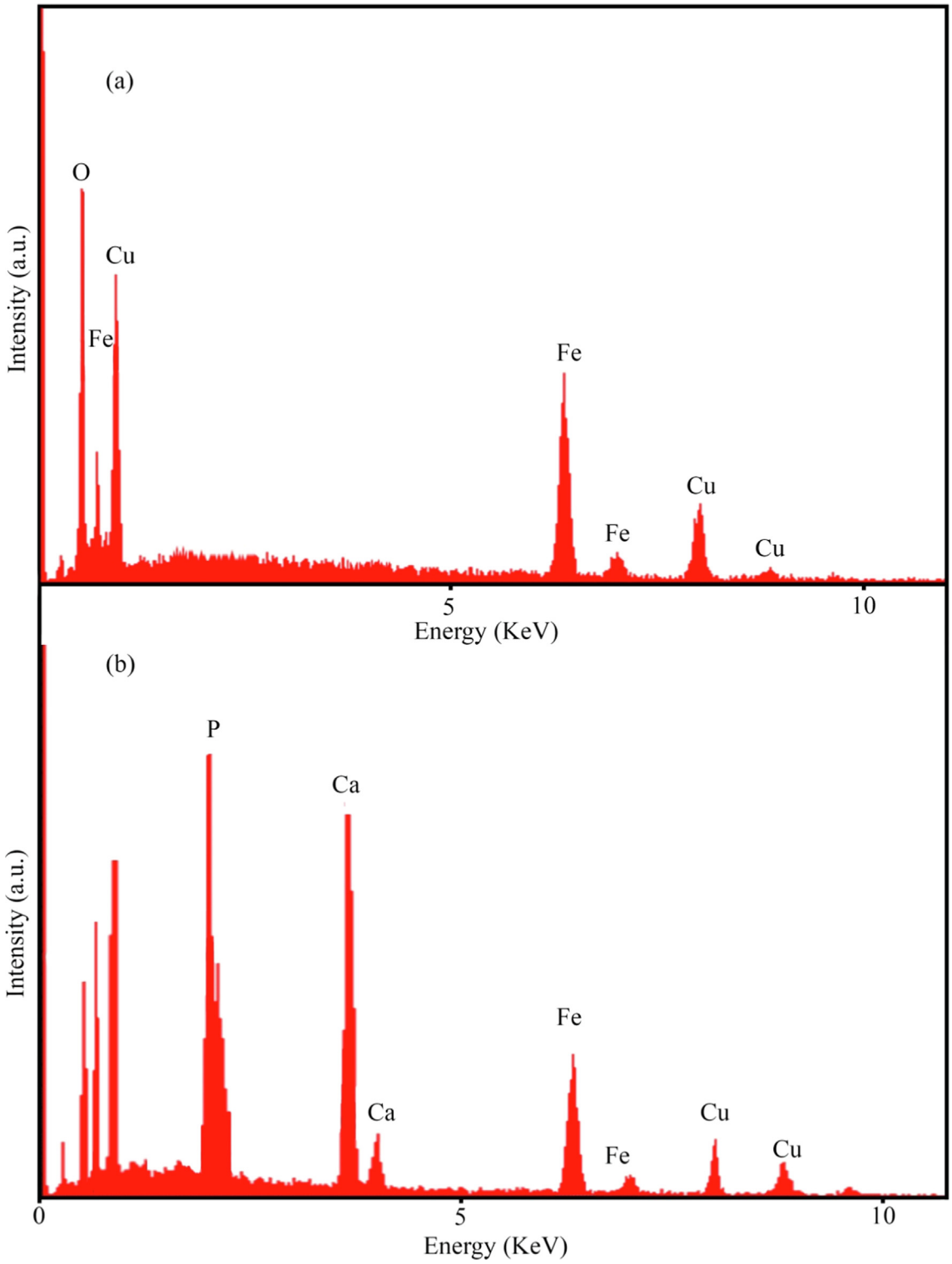

Fig. 6 EDS spectrum of (a) $CuFe_{12}O_{19}$, and (b) $CuFe_{12}O_{19}$@HAp MNCs.

MNCs, respectively. The zeta-potential results showed that the prepared $CuFe_{12}O_{19}$@HAp-APTES NCs dispersed in water because of the large electrostatic repulsive forces between the particles. After deposition of hydroxyapatite on the surface of $CuFe_{12}O_{19}$, the values of zeta potential decreased. This exhibited less stability because of the low electrostatic repulsive forces between synthesized particles (Salunkhe et al., 2016). Fig. 7b shows the specific surface area and pore size distribution measured by nitrogen adsorption–desorption isotherm. The $CuFe_{12}O_{19}$@HAp-APTES MNCs showed a similar type

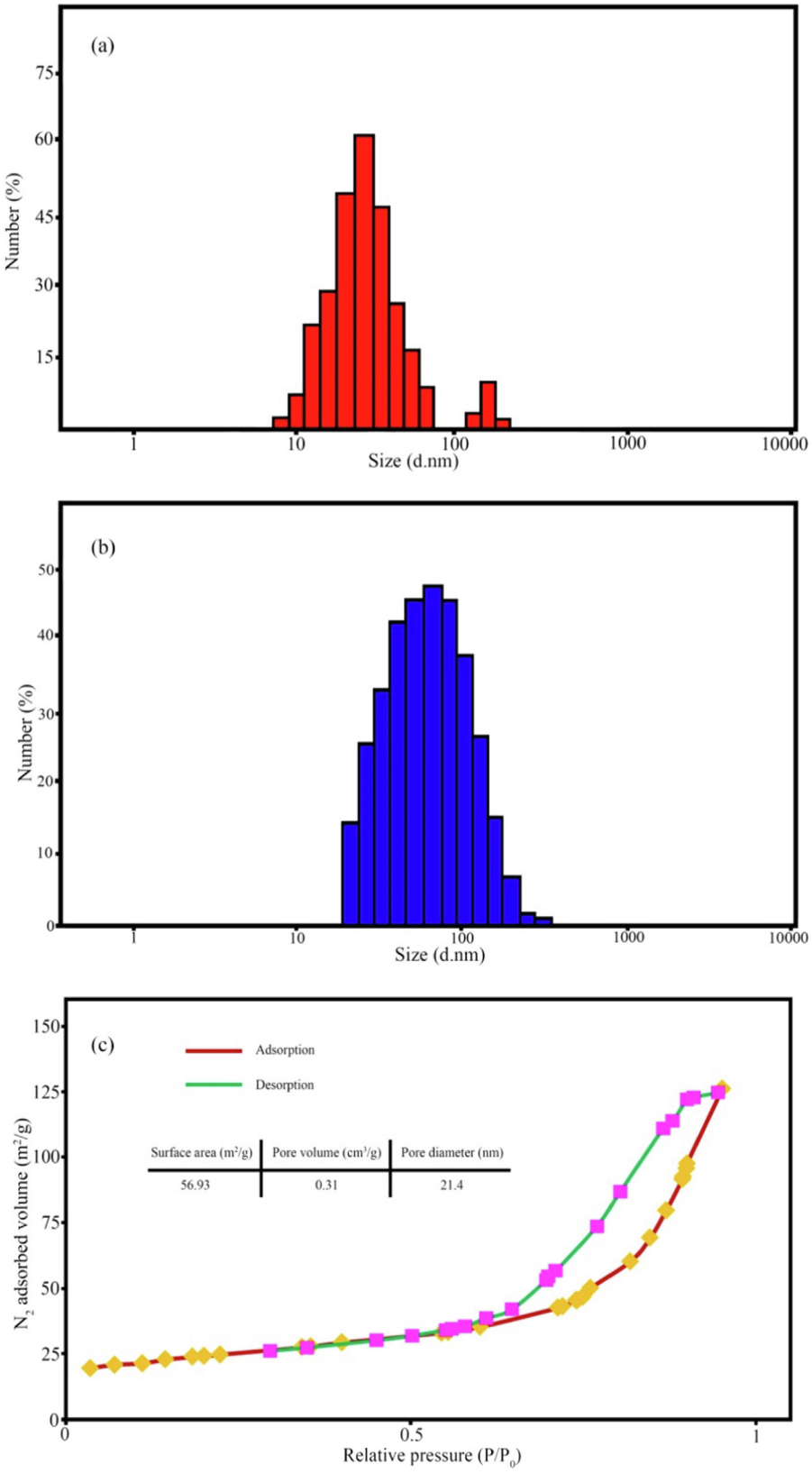

Fig. 7 DLS plots of (a) $CuFe_{12}O_{19}$, (b) $CuFe_{12}O_{19}$@HAp-APTES MNCs, and (c) N_2 adsorption–desorption isotherms for $CuFe_{12}O_{19}$@HAp-APTES MNCs.

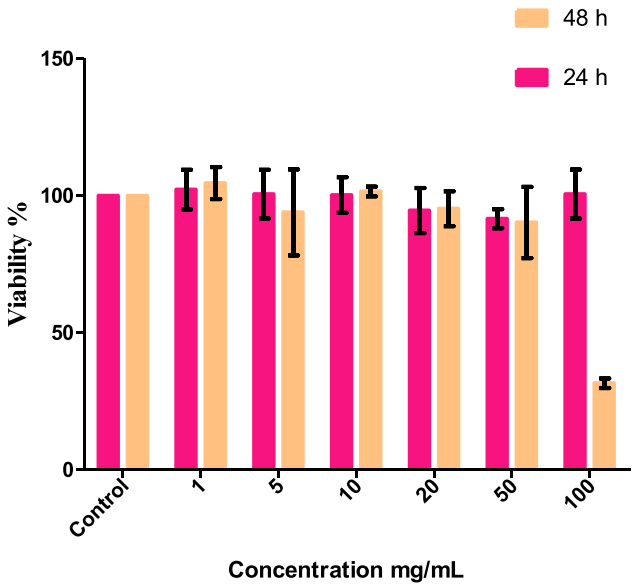

Fig. 8 MTT assay: HEK-293 cell was exposed to the ATL-$CuFe_{12}O_{19}$@HAp-APTES MNCs for 24 and 48 h.

of IV isotherm according to the International Union of Pure and Applied Chemistry (IUPAC) classification which exhibits their mesoporous nature (Thommes et al., 2015).

3.6. Cytotoxicity

Fig. 8 reveals the evaluation of cell viability of ATL-$CuFe_{12}O_{19}$@HAp-APTES MNCs on HEK-293 normal cell lines at various concentrations after 24 and 48 h. Statistical analysis exhibited no cytotoxicity for ATL-$CuFe_{12}O_{19}$@HAp-APTES MNCs at 24 h compared to the untreated control. In our previous study (Mortazavi-Derazkola et al., 2017), we published that pure atenolol showed significant toxicity on the HEK-293 cell line at 100 mg/mL concentration after 24 h. Furthermore, cytotoxicity study showed (after 48 h) that ATL-$CuFe_{12}O_{19}$@HAp-APTES MNCs present significant toxicity at 100 mg/mL, in comparison to the toxicity of atenolol at 50 and 100 mg/mL. In-vitro toxicity results showed that loading drug into $CuFe_{12}O_{19}$@HAp-APTES MNCs reduces the toxicity of the pure drug.

3.7. Drug loading and release

The percentage of atenolol loading on sample carriers ($CuFe_{12}O_{19}$@HAp-APTES MNCs) was analyzed using UV–vis over 200–800 nm. Entrapment efficiency (EE) is a crucial parameter for the determination of nanocarriers. The percentage entrapment efficiency (Eq. (1)) was calculated from the following equations:

$$\textit{Entrapment efficiency}\,(\%) = \frac{\textit{Weight of initial atenolol} - \textit{Weight of free atenolol}}{\textit{Weight of initial atenolol}} \times 100 \quad (1)$$

According to the entrapment efficiency equation, the percentage of entrapment efficiency for $CuFe_{12}O_{19}$@HAp MNCs and $CuFe_{12}O_{19}$@HAp-APTES MNCs was measured as 21.7 % and 63.1 %, respectively. The entrapment efficiency of $CuFe_{12}O_{19}$@HAP-APTES MNCs was more than pure $CuFe_{12}O_{19}$@HAp MNCs. This increase can be related to the N—H (amino) groups (from APTES) linked to the hydroxyl walls of the hydroxyapatite structure. The mechanism of functionalization of $CuFe_{12}O_{19}$@HAp MNCs with APTES and the interaction of these compounds with atenolol were shown in Scheme.1. The in-vitro release of atenolol from the synthesized $CuFe_{12}O_{19}$@HAp MNCs and $CuFe_{12}O_{19}$@HAp-APTES MNCs was carried out in simulated body fluid (FBS) with different pH values (intestinal pH value of 5.8–6.7 and stomach pH value of 1.5–2). Fig. 9 depicts the cumulative release of atenolol from $CuFe_{12}O_{19}$@HAp MNCs and $CuFe_{12}O_{19}$@HAp-APTES MNCs at various times. A rapid drug release was observed initially (53.4 % for $CuFe_{12}O_{19}$@-HAp MNCs and 24.8 % for $CuFe_{12}O_{19}$@HAp-APTES MNCs). This initial burst can be interpreted as follows: in the beginning, the immediate dissolution of atenolol molecules located close to the surface of nanocarrier occurs, while the drug molecules captured in the pores need more time to escape

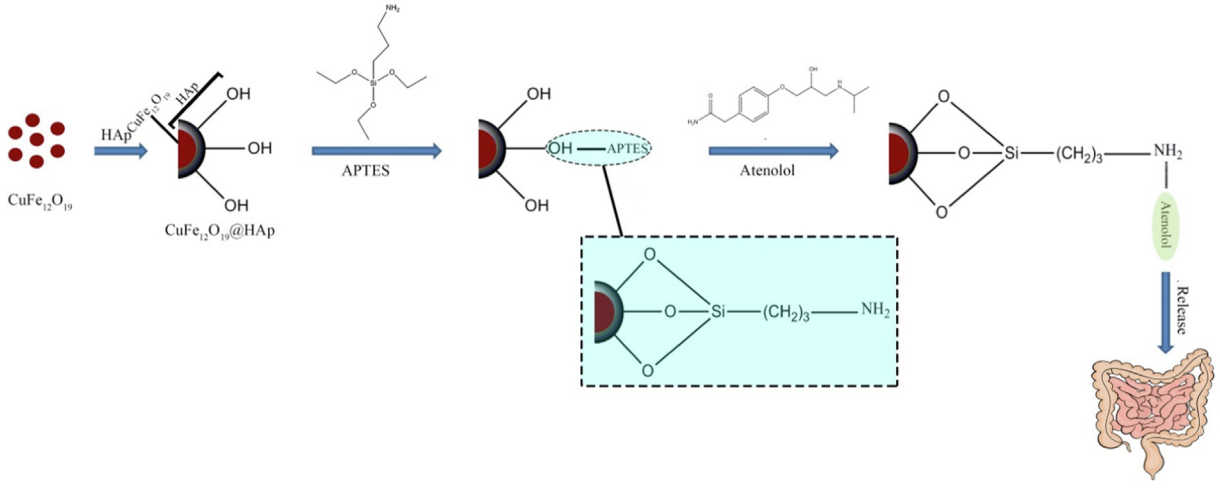

Scheme 1 Schematic illustration of the preparation of $CuFe_{12}O_{19}$@HAp-APTES MNCs and atenolol loaded magnetic nanocomposites.

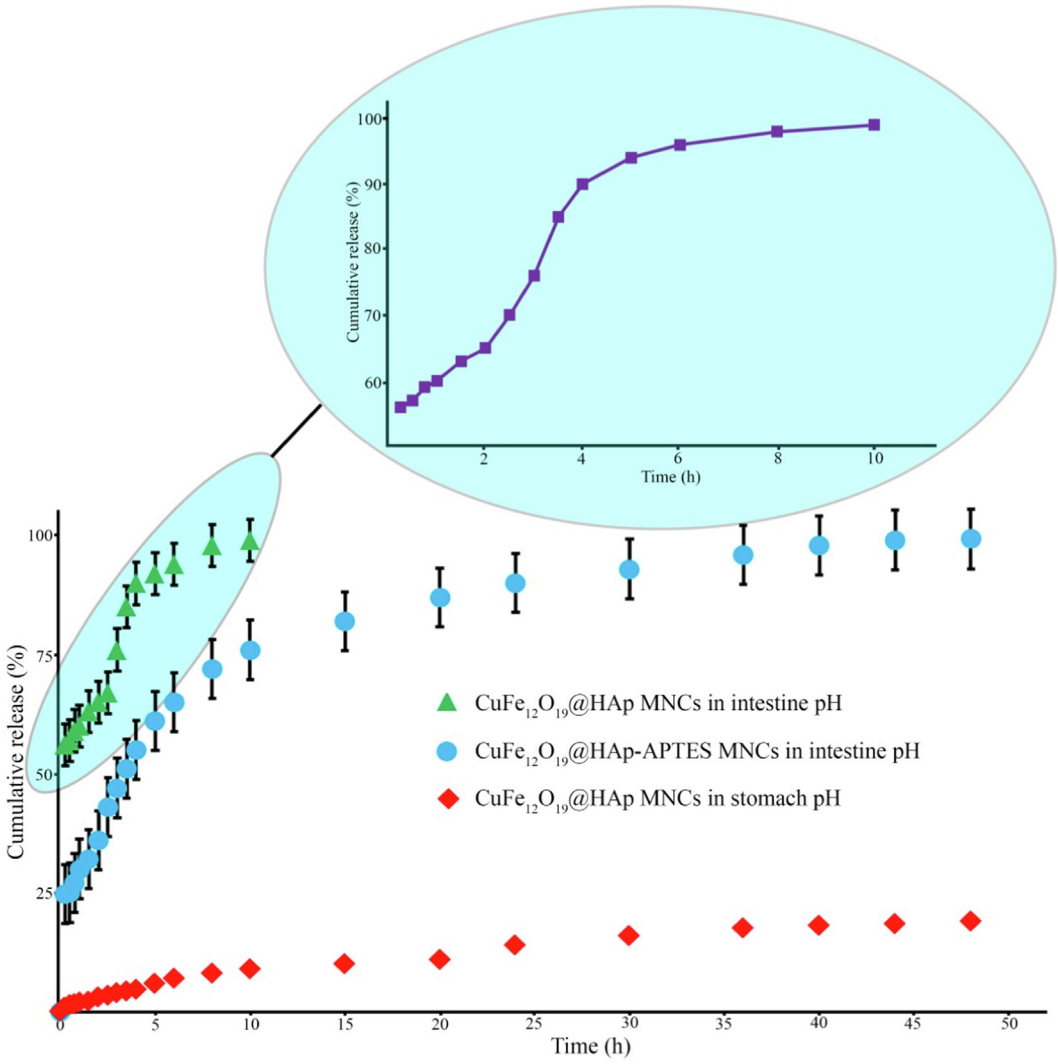

Fig. 9 In-vitro drug release profiles from magnetic nanocomposites in stomach and intestine environment.

from the pores. In other words, this difference was due to the stronger interaction of the drug molecule to the amine (in $CuFe_{12}O_{19}$@HAp-APTES MNCs) compared to the hydroxyl group (in $CuFe_{12}O_{19}$@HAp MNCs). Examination of gastric pH showed that no significant release occurred within 48 h. In-vitro atenolol release behavior of nanocomposites was performed in intestinal pH value. According to Fig. 9, the efficiency of the atenolol release in the intestine pH-similar milieu after 48 h was 98.3 % for $CuFe_{12}O_{19}$@HAp-APTES MNCs. Thus, $CuFe_{12}O_{19}$@HAp-APTES MNCs revealed a pH-responsive behavior and slow atenolol in-vitro release over a period of about 48 h. In contrast, the whole drug was released from pure $CuFe_{12}O_{19}$@HAp MNCs after 10 h. In general, it can be concluded that the functional group plays a critical role in the drug delivery system. Kermanian and co-authors synthesized magnetite nanoparticles dispersed on the hydroxyapatite with a hydrothermal method. Then, IO-HA nanocomposites were used as a nanocarrier for the delivery of curcumin. Their results showed that the synthesized magnetic nanocomposites were non-cytotoxic and hemocompatible, as well as an excellent pH-sensitive drug carrier (Kermanian et al., 2020). Foroughi *et al.,* synthesized hydroxyapatite-$MgFe_2O_4$ nanocomposite by a one-step reverse microemulsion route and applied as a magnetic drug delivery system. They investigated the effect of calcination temperature on the efficiency of drug release. The results displayed that the calcination temperature was effective in the drug delivery rate of hydroxyapatite-$MgFe_2O_4$ nanocomposite (Foroughi et al., 2016).

4. Conclusion

In summary, $CuFe_{12}O_{19}$@HAp-APTES MNCs were synthesized through ultrasound-assisted precipitation method, which innovatively used as a nanocarrier to loading and release atenolol as a suitable drug for hypertensive patients. The structure, elemental composition and size of products were determined by FESEM, TEM, DLS, VSM, BET, EDS, FT-IR, XRD, and UV–vis spectra. The VSM and TEM results show that $CuFe_{12}O_{19}$@HAp-APTES MNCs have a superparamagnetic properties with spherical and rod morphologies. The NH_2 group was incorporated into the hydroxyapatite and applied as atenolol delivery carriers. The atenolol drug was successfully entrapped with the efficiency of 63.1 %. In vitro atenolol release was determined (in

simulated body fluid) and the maximum percentage drug release was 98.3 % after 48 h. Overall, the burst release and sustained release can be related to the atenolol present on the surface of the nanocomposites and the captured atenolol within the pores, respectively.

Acknowledgment

In this investigation, the entire procedures were conducted according to the Helsinki Declaration and ethical standards of the institutional research committee. The ethics code was taken from Birjand University of Medical Sciences (IR.BUMS.REC.1399.132).

References

Abbasi Aval, N., Pirayesh Islamian, J., Hatamian, M., Arabfirouzjaei, M., Javadpour, J., Rashidi, M.R., 2016. Doxorubicin loaded large-pore mesoporous hydroxyapatite coated superparamagnetic Fe_3O_4 nanoparticles for cancer treatment. Int. J. Pharm. 509, 159–167.

Adhikari, S.N., Nayak, B.S., Nayak, A.K., Mohanty, B., 2010. Formulation and evaluation of buccal patches for delivery of atenolol. AAPS PharmSciTech 11, 1038–1044.

Amiri, M., Salavati-Niasari, M., Pardakhty, A., Ahmadi, M., Akbari, A., 2017. Caffeine: A novel green precursor for synthesis of magnetic $CoFe_2O_4$ nanoparticles and pH-sensitive magnetic alginate beads for drug delivery. Mater. Sci. Eng., C 76, 1085–1093.

Ansari, F., Soofivand, F., Salavati-Niasari, M., 2015. Utilizing maleic acid as a novel fuel for synthesis of $PbFe_{12}O_{19}$ nanoceramics via sol–gel auto-combustion route. Mater. Charact. 103, 11–17.

Ansari, F., Sobhani, A., Salavati-Niasari, M., 2016. Facile synthesis, characterization and magnetic property of $CuFe_{12}O_{19}$ nanostructures via a sol–gel auto-combustion process. J. Magn. Magn. Mater. 401, 362–369.

Asgari, M., Miri, T., Soleymani, M., Barati, A., 2021. A novel method for in situ encapsulation of curcumin in magnetite-silica core-shell nanocomposites: A multifunctional platform for controlled drug delivery and magnetic hyperthermia therapy. J. Mol. Liq. 324, 114731.

Cueto-Díaz, E.J., Castro-Muñiz, A., Suárez-García, F., Gálvez-Martínez, S., Torquemada-Vico, M.C., Valles-González, M.P., Mateo-Martí, E., 2021. APTES-Based Silica Nanoparticles as a Potential Modifier for the Selective Sequestration of CO(2) Gas Molecules. Nanomaterials (Basel, Switzerland) 11.

Darwish, M.S.A., Kim, H., Lee, H., Ryu, C., Lee, J.Y., Yoon, J., 2019. Synthesis of Magnetic Ferrite Nanoparticles with High Hyperthermia Performance via a Controlled Co-Precipitation Method. Nanomaterials (Basel, Switzerland) 9.

Ebrahimzadeh, M.A., Hashemi, Z., Mohammadyan, M., Fakhar, M., Mortazavi-Derazkola, S., 2021. In vitro cytotoxicity against human cancer cell lines (MCF-7 and AGS), antileishmanial and antibacterial activities of green synthesized silver nanoparticles using Scrophularia striata extract. Surf. Interfaces 23, 100963.

Fekri, M.H., Soleymani, S., Mehr, M.R., Akbari-adergani, B., 2022. Synthesis and characterization of mesoporous ZnO/SBA-16 nanocomposite: Its efficiency as drug delivery system. J. Non-Cryst. Solids 591, 121512.

Foroughi, F., Hassanzadeh-Tabrizi, S.A., Bigham, A., 2016. In situ microemulsion synthesis of hydroxyapatite-$MgFe_2O_4$ nanocomposite as a magnetic drug delivery system. Mater. Sci. Eng., C 68, 774–779.

Hashemi, Z., Mizwari, Z.M., Mohammadi-Aghdam, S., Mortazavi-Derazkola, S., Ali Ebrahimzadeh, M., 2022. Sustainable green synthesis of silver nanoparticles using Sambucus ebulus phenolic extract (AgNPs@SEE): Optimization and assessment of photocatalytic degradation of methyl orange and their in vitro antibacterial and anticancer activity. Arabian J. Chem. 15, 103525.

Hassanzadeh-Tabrizi, S.A., Norbakhsh, H., Pournajaf, R., Tayebi, M., 2021. Synthesis of mesoporous cobalt ferrite/hydroxyapatite core-shell nanocomposite for magnetic hyperthermia and drug release applications. Ceram. Int. 47, 18167–18176.

Herrault, F., Cui, S., Guan, X.N., Gross, A.F., 2021. Synthesis and binder-free assembly of $SrFe_{12}O_{19}$ nano-platelets for wafer-scale patterning of magnetic components. Microelectron. Eng. 236, 111467.

Hışır, A., Karaoğlan, G.K., Avcıata, O., 2022. Synthesis of tetracarboxy phthalocyanines modified TiO_2 nanocomposite photocatalysts and investigation of photocatalytic decomposition of organic pollutant methylene blue under visible light. J. Mol. Struct. 1266, 133498.

Kaur, P., Singh, S., Renu, J., Kumar, V., Tikoo, K.B., Kaushik, A., Singhal, S., 2022. Development of emphatic catalysts for waste water remediation via synchronized free radical and non-free radical routes with composites of strontium hexaferrite, graphene and multi-walled carbon nanotubes. Ceram. Int. 48, 4795–4811.

Kermanian, M., Naghibi, M., Sadighian, S., 2020. One-pot hydrothermal synthesis of a magnetic hydroxyapatite nanocomposite for MR imaging and pH-Sensitive drug delivery applications. Heliyon 6, e04928.

Khan, K., Batool, Z., Manzoor, S., Ahmad, D., Aman, S., Alhashmialameer, D., Abd El-Gawad, H.H., Taha, T.A., Ashiq, M.N., 2022. Fabrication of substituted Y-type hexaferrites/carbon dots composites for recording media and photodegradation of dye. Ceram. Int. 48, 27550–27559.

Khoobi, A., Salavati-Niasari, M., Amiri, O., 2021. Sol-gel auto-combustion synthesis and characterization of $ZnFe_{12}O_{19}$ as a nanosorbent using fructose for HPLC-UV determination of betaxolol in biological samples. J. Alloy. Compd. 853, 157393.

Khormali, K., Mizwari, Z.M., Masoumeh Ghoreishi, S., Mortazavi-Derazkola, S., Khezri, B., 2021. Novel Dy_2O_3/ZnO-Au ternary nanocomposites: Green synthesis using pomegranate fruit extract, characterization and their photocatalytic and antibacterial properties. Bioorg. Chem. 115, 105204.

Khushbu, R., 2021. Jindal, RSM-CCD optimized microwave assisted synthesis of chitosan and sodium alginate based nanocomposite containing inclusion complexes of β-cyclodextrin and amlodipine besylate for sustained drug delivery systems. J. Drug Delivery Sci. Technol. 61, 102325.

Mahdiani, M., Soofivand, F., Ansari, F., Salavati-Niasari, M., 2018. Grafting of $CuFe_{12}O_{19}$ nanoparticles on CNT and graphene: Eco-friendly synthesis, characterization and photocatalytic activity. J. Cleaner Prod. 176, 1185–1197.

Mohammadi, R., Saboury, A., Javanbakht, S., Foroutan, R., Shaabani, A., 2021. Carboxymethylcellulose/polyacrylic acid/starch-modified Fe_3O_4 interpenetrating magnetic nanocomposite hydrogel beads as pH-sensitive carrier for oral anticancer drug delivery system. Eur. Polym. J. 153, 110500.

Mohammadzadeh, P., Shafiee Ardestani, M., Mortazavi-Derazkola, S., Bitarafan-Rajabi, A., Ghoreishi, S.M., 2019. PEG-Citrate dendrimer second generation: is this a good carrier for imaging agents In Vitro and In Vivo? IET nanobiotechnology 13, 560–564.

Mortazavi-Derazkola, S., Naimi-Jamal, M.R., Ghoreishi, S.M., 2016. Synthesis, Characterization, and Atenolol Delivery Application of Functionalized Mesoporous Hydroxyapatite Nanoparticles Prepared by Microwave-Assisted Co-precipitation Method. Curr. Drug Deliv. 13, 1123–1129.

Mortazavi-Derazkola, S., Salavati-Niasari, M., Khojasteh, H., Amiri, O., Ghoreishi, S.M., 2017. Green synthesis of magnetic Fe_3O_4/SiO_2/HAp nanocomposite for atenolol delivery and in vivo toxicity study. J. Cleaner Prod. 168, 39–50.

Mushtaq, A., Zhao, R., Luo, D., Dempsey, E., Wang, X., Iqbal, M.Z., Kong, X., 2021. Magnetic hydroxyapatite nanocomposites: The advances from synthesis to biomedical applications. Mater. Des. 197, 109269.

Naghizadeh, A., Mizwari, Z.M., Ghoreishi, S.M., Lashgari, S., Mortazavi-Derazkola, S., Rezaie, B., 2021. Biogenic and eco-benign synthesis of silver nanoparticles using jujube core extract and its performance in catalytic and pharmaceutical applications: Removal of industrial contaminants and in-vitro antibacterial and anticancer activities. Environ. Technol. Innovation 23, 101560.

Nezami, S., Sadeghi, M., Mohajerani, H., 2020. A novel pH-sensitive and magnetic starch-based nanocomposite hydrogel as a controlled drug delivery system for wound healing. Polym. Degrad. Stab. 179, 109255.

Orooji, Y., Mortazavi-Derazkola, S., Ghoreishi, S.M., Amiri, M., Salavati-Niasari, M., 2020. Mesopourous Fe_3O_4@SiO_2-hydroxyapatite nanocomposite: Green sonochemical synthesis using strawberry fruit extract as a capping agent, characterization and their application in sulfasalazine delivery and cytotoxicity. J. Hazard. Mater. 400, 123140.

Saejung, C., Raksapon, D., Chaiyarat, A., 2022. Synthesis and application of a magnetically recoverable biological nanocomposite material for waste cooking oil removal and commercial product recovery in wastewater treatment. J. Cleaner Prod. 363, 132425.

Sağir, T., Huysal, M., Durmus, Z., Kurt, B.Z., Senel, M., Isık, S., 2016. Preparation and in vitro evaluation of 5-flourouracil loaded magnetite-zeolite nanocomposite (5-FU-MZNC) for cancer drug delivery applications. Biomedicine & pharmacotherapy = Biomedecine & pharmacotherapie 77, 182–190.

Saire-Saire, S., Garcia-Segura, S., Luyo, C., Andrade, L.H., Alarcon, H., 2020. Magnetic bio-nanocomposite catalysts of $CoFe_2O_4$/hydroxyapatite-lipase for enantioselective synthesis provide a framework for enzyme recovery and reuse. Int. J. Biol. Macromol. 148, 284–291.

Salahuddin, N., Abdelwahab, M., Gaber, M., Elneanaey, S., 2020. Synthesis and Design of Norfloxacin drug delivery system based on PLA/TiO2 nanocomposites: Antibacterial and antitumor activities. Mater. Sci. Eng., C 108, 110337.

Salimi, E., 2021. Development of bioactive sodium alginate/sulfonated polyether ether ketone/hydroxyapatite nanocomposites: Synthesis and in-vitro studies. Carbohydr. Polym. 267, 118236.

Salunkhe, A.B., Khot, V.M., Ruso, J.M., Patil, S.I., 2016. Water dispersible superparamagnetic Cobalt iron oxide nanoparticles for magnetic fluid hyperthermia. J. Magn. Magn. Mater. 419, 533–542.

Shafiee, S., Ahangar, H.A., Saffar, A., 2019. Taguchi method optimization for synthesis of Fe_3O_4 @chitosan/Tragacanth Gum nanocomposite as a drug delivery system. Carbohydr. Polym. 222, 114982.

Shirzadi-Ahodashti, M., Mortazavi-Derazkola, S., Ebrahimzadeh, M. A., 2020. Biosynthesis of noble metal nanoparticles using crataegus monogyna leaf extract (CML@X-NPs, X= Ag, Au): Antibacterial and cytotoxic activities against breast and gastric cancer cell lines. Surf. Interfaces 21, 100697.

Shirzadi-Ahodashti, M., Ebrahimzadeh, M.A., Amiri, O., Naghizadeh, A., Mortazavi-Derazkola, S., 2020. Novel NiFe/Si/Au magnetic nanocatalyst: Biogenic synthesis, efficient and reusable catalyst with enhanced visible light photocatalytic degradation and antibacterial activity. Appl. Organomet. Chem. 34, e5467.

Shirzadi-Ahodashti, M., Ebrahimzadeh, M.A., Ghoreishi, S.M., Naghizadeh, A., Mortazavi-Derazkola, S., 2020. Facile and eco-benign synthesis of a novel $MnFe_2O_4$@SiO_2@Au magnetic nanocomposite with antibacterial properties and enhanced photocatalytic activity under UV and visible-light irradiations. Appl. Organomet. Chem. 34, e5614.

Shirzadi-Ahodashti, M., Mizwari, Z.M., Hashemi, Z., Rajabalipour, S., Ghoreishi, S.M., Mortazavi-Derazkola, S., Ebrahimzadeh, M. A., 2021. Discovery of high antibacterial and catalytic activities of biosynthesized silver nanoparticles using C. fruticosus (CF-AgNPs) against multi-drug resistant clinical strains and hazardous pollutants. Environ. Technol. Innovation 23, 101607.

Taufiq, A., Nikmah, A., Hidayat, A., Sunaryono, S., Mufti, N., Hidayat, N., Susanto, H., 2020. Synthesis of magnetite/silica nanocomposites from natural sand to create a drug delivery vehicle. Heliyon 6, e03784.

Thadikonda, K.P., Lau-Cam, C.A., Thadikonda, V.L., Theofanopoulos, V., 1995. Nasal Delivery of Atenolol and Timolol in the Rat and the Effect of Absorption Enhancers. Drug Dev. Ind. Pharm. 21, 349–360.

Thangaraj, V., Chang, J.-H., Dash, C.S., Sundararajan, M., Mohanraj, K., Ahmad, N., Alshehri, A.M., Mathankumar, K., Sumathi, S., Yuvaraj, S., Arun, A., 2022. Study of structural, optical, antibacterial, anticancer effects on MDA-MB-231 cell line and drug delivery characteristics of novel $Ce_{4-x}Cs_{2(1+x)}Fe_{5-x}ZnxO_{14+\delta}$ [$0 \leq x \leq 0.45$] nanocomposite prepared via sol-gel synthesis technique. Surf. Interfaces 29, 101746.

Thirupathy, C., Cathrin Lims, S., John Sundaram, S., Mahmoud, A. H., Kaviyarasu, K., 2020. Equilibrium synthesis and magnetic properties of $BaFe_{12}O_{19}$/$NiFe_2O_4$ nanocomposite prepared by co precipitation method. Journal of King Saud University - Science 32, 1612–1618.

Thommes, M., Kaneko, K., Neimark, A.V., Olivier, J.P., Rodriguez-Reinoso, F., Rouquerol, J., Sing, K.S.W., 2015. Physisorption of gases, with special reference to the evaluation of surface area and pore size distribution (IUPAC Technical Report). Pure Appl. Chem. 87.

Tian, B., Tang, S., Wang, C.-D., Wang, W.-G., Wu, C.-L., Guo, Y.-J., Guo, Y.-P., Zhu, Z.-A., 2014. Bactericidal properties and biocompatibility of a gentamicin-loaded Fe_3O_4/carbonated hydroxyapatite coating. Colloids Surf., B 123, 403–412.

Wei, W., Ding, Y., Zhao, A., Ge, K., Zhang, C., Li, Y., Zhang, J., Jia, G., 2017. Monodisperse and mesoporous walnut kernel-like SiO_2/γ-Fe_2O_3 nanocomposite: Synthesis, magnetic properties, and application in drug delivery. J. Alloy. Compd. 728, 585–591.

Yang, Z.-P., Gong, X.-Y., Zhang, C.-J., 2010. Recyclable Fe_3O_4/hydroxyapatite composite nanoparticles for photocatalytic applications. Chem. Eng. J. 165, 117–121.

Zhang, J., Jia, G., Wang, J., Kong, H., Li, H., Zhang, C., 2022. Hollow chain-like SiO2/ZnO nanocomposites: Electrospinning synthesis, defect-related luminescence, and applications for drug delivery. Colloids Surf., A 647, 129139.